Nonadiabatic reactive scattering of hydrogen on different surface facets of copper

Wojciech G. Stark [1], Connor L. Box [1], Matthias Sachs [2], Nils Hertl [1,3] and Reinhard J. Maurer [1,3,*]

[1] *Department of Chemistry, University of Warwick, Coventry CV4 7AL, United Kingdom*

[2] *School of Mathematics, University of Birmingham, Birmingham B15 2TS, United Kingdom*

[3] *Department of Physics, University of Warwick, Coventry CV4 7AL, United Kingdom*

(Received 23 May 2025; accepted 20 June 2025; published 21 July 2025)

Dissociative chemisorption is a key process in hydrogen-metal surface chemistry, where nonadiabatic effects caused by low-lying electron-hole-pair excitations may affect reaction outcomes. Molecular dynamics with electronic friction simulations can capture weak nonadiabatic effects at metal surfaces, but require energy landscapes and electronic friction tensors as input. Here, we present full-dimensional machine learning surrogate models of the electronic friction tensor to study reactive hydrogen chemistry at the low-index surface facets Cu(100), Cu(110), Cu(111), and Cu(211). We combine these surrogate models with machine learning interatomic potentials to simulate quantum-state-resolved H_2 reactive scattering on pristine copper surfaces. The predicted sticking coefficient and survival probabilities are in excellent agreement with experiments. Comparison between adiabatic and nonadiabatic simulations reveals that the influence of electron-hole pair excitations on the scattering dynamics is weak, and that the probability for dissociative adsorption is dominated by the shape of the underlying potential energy surface and the initial vibrational quantum state. Nonadiabatic effects only lead to subtle changes in rovibrationally inelastic state-to-state scattering probabilities. The differences between jellium-based isotropic local density friction and full *ab initio* response-theory-based orbital-dependent friction are even more subtle. The presented machine learning models represent the most accurate publicly available, full-dimensional models for H_2 on copper to date.

DOI: 10.1103/h7vd-94pk

I. INTRODUCTION

Dissociative adsorption of hydrogen on metal surfaces plays a vital role in many crucial processes, such as heterogeneous catalysis [1], production of molecular hydrogen [2], olefin hydrogenation [3], hydrogen storage [4], and many others [5–8]. At the atomic level, these macroscopic processes involve a complex reaction network, rendering the detailed characterization of individual elementary steps highly challenging [9].

To better isolate specific elementary steps in gas-surface dynamics, experiments and simulations are commonly performed at idealized single-crystal surfaces. The incoming gaseous particles are prepared in well-defined vibrational and rotational quantum states. In combination with quantum-state selective measurement techniques, such as resonance enhanced multiphonon ionization (REMPI), and angular-resolved time-of-flight measurements, it is possible to realize detailed state-to-state scattering experiments [10]. These experiments are useful in scrutinizing the scattering dynamics of the impinging molecules and the concomitant energy transfer from the molecule to the surface, as well as the intramolecular energy redistribution. The dynamics of hydrogen molecules on metal surfaces are particularly intriguing: Many metal catalysts readily catalyze H_2 dissociation, enabling the catalytic processes outlined above [11]. The light mass of hydrogen means that nuclear quantum effects likely also play a role in gas-surface dynamics. [12] Additionally, for metallic substrates, the scattering process can be affected by nonadiabatic effects and energy dissipation processes that arise as a result of the excitation of electron-hole pairs (ehps) in the metal. These effects have the potential to modify reaction outcomes [13–15]. Hence, quantum-state resolved H_2 scattering from pristine metal surfaces constitutes an ideal stress test for existing concepts in quantum mechanics and theoretical gas-surface dynamics and the prediction capabilities of first principles simulation methods [16].

Over the last decades, H_2 on copper surfaces has become a commonly studied model system when it comes to quantum-state resolved dissociative adsorption [17–24] and the concomitant kinetics [25–28] as well as associative desorption dynamics of diatomic molecules from metal surfaces [29–34]. A key finding that emerged from the vast literature is that vibrational excitation of H_2 significantly promotes its dissociation on copper. The extent to which vibrational excitation promotes surface dissociation reactions is typically quantified by the vibrational efficacy [35]. This quantification attempt took inspiration from the well-known Polanyi rules [36], which connect the ability to overcome the reaction barrier through vibrational excitation with the shape of the

*Contact author: r.maurer@warwick.ac.uk

Published by the American Physical Society under the terms of the Creative Commons Attribution 4.0 International license. Further distribution of this work must maintain attribution to the author(s) and the published article's title, journal citation, and DOI.

reaction pathway for reactions of the type A + BC → AB + C: Reactions with barriers that appear early on the pathway can be promoted by increasing the translational energy. Reactions with late barriers, on the other hand, are promoted by vibrational excitations.

While most computational studies of H_2 interacting with copper surfaces have been performed within the Born-Oppenheimer approximation (BOA), this framework assumes that the nuclear dynamics evolve solely on the ground-state potential energy surface (PES). The BOA generally holds for systems with well-separated electronic states; however, at metal surfaces, particularly under vibrational excitation, this assumption does not generally hold. This is well documented for systems such as NO and CO scattering from Au(111) and Ag(111), where electronic excitations can substantially influence reaction dynamics [37–40].

For H_2 on copper, the possibility of energy dissipation into ehp excitations has motivated studies beyond the BOA, particularly using molecular dynamics with electronic friction (MDEF) [41]. Within this framework, most previous work on gas-surface scattering has relied on the local density friction approximation (LDFA) [42,43], which models friction as an isotropic function of the local electron density. While LDFA-based simulations generally report only a weak impact of nonadiabatic effects on the sticking probability of H_2 on copper [43,44], the method's applicability to molecular scattering has been questioned—both for its reliance on isotropic damping and for its grounding in jellium-based models rather than *ab initio* electronic structure calculations [45,46].

Electronic friction tensors (EFTs) have also been calculated directly from density functional theory (DFT) via first-order time-dependent perturbation theory (TDPT) [41,45,47]. This approach is also called orbital-dependent friction (ODF). The resulting friction tensors are fully anisotropic and capture coordinate and mode-dependent differences in nonadiabatic relaxation during atom and molecule dynamics at surfaces [48–51], including hydrogen atom scattering [52].

Spiering and Meyer [15] identified vibrational de-excitation from $H_2(v = 2, J = 1) \rightarrow H_2(v = 1, J = 1)$ of H_2 on Cu(111) as an observable that may be particularly sensitive to nonadiabatic effects. Their comparison between LDFA and ODF revealed a distinct kinetic energy dependence of vibrational de-excitation probability that only arises when full tensorial and anisotropic electronic friction effects are considered. However, their model was restricted to six dimensions, one surface facet, and neglected thermal surface motion, limiting its generality.

Recent advances in machine learning interatomic potentials (MLIPs) enable the efficient simulation of gas-surface reaction probabilities, considering all degrees of freedom, including surface phonons [53–56]. Such models, among several other systems, have recently been proposed for a variety of systems, including reactive H_2 scattering on various facets of copper [57–59]. To efficiently perform MDEF simulations with MLIPs, high-dimensional configuration-dependent representations of the EFT are required. Such representations have been recently proposed [60,61] and applied to systems such as NO on Au(111) [46]. In particular, the general model proposed by Sachs *et al.* [61] is appealing as it is based on a rotationally equivariant atomic cluster expansion [62,63] construction that is intrinsically transferable and size extensible, enabling the representation and evaluation of friction across configurational space. With the emergence of the above-mentioned ML surrogate models, comparative studies of nonadiabatic surface chemistry across different surface facets become possible.

In this work, we present high-dimensional machine learning surrogate models of EFTs for H_2 on four surface facets of copper based on LDFA and ODF. Upon careful validation of the EFT models, we combine them with a recently developed transferable MLIP for reactive surface chemistry of H_2 on copper [58,59] to perform MDEF simulations of H_2 state-to-state scattering across four surface facets of copper: Cu(111), Cu(100), Cu(110), Cu(211). The models accurately account for phononic and electronic energy dissipation effects during scattering and achieve excellent agreement with previously reported experimental sticking and survival probabilities of the initial quantum states across different facets. The presented and provided models therefore represent the—to date—most accurate PES and EFT models for reactive hydrogen chemistry on copper. Comprehensive scattering simulations reveal that the impact of electronic nonadiabaticity on reaction probabilities is weak across all surface facets, which is in line with previous findings [43,44,64]. Notably, only a weak kinetic energy dependence of the vibrational de-excitation from $H_2(v = 2, J = 1) \rightarrow H_2(v = 1, J = 1)$ is found, with nonadiabatic effects only changing absolute populations by a fraction of a percent. Thus, a measurable signature of nonadiabaticity is unlikely to be found on Cu(111) or any one of the other studied low-index surface facets.

II. METHODS

A. Molecular dynamics with electronic friction

The motion of atoms in molecular dynamics with electronic friction (MDEF) follows the following Langevin equation:

$$M_i \ddot{R}_i = -\frac{\partial V(\boldsymbol{R}, \boldsymbol{z})}{\partial R_i} - \sum_j \Lambda_{ij}(\boldsymbol{R}, \boldsymbol{z}) \dot{R}_j + F_i^{\mathcal{R}}(t), \quad (1)$$

where the atomic coordinate i, has mass M_i and position R_i. $V(\boldsymbol{R}, \boldsymbol{z})$ is the potential energy of the simulated atomistic system. $\Lambda_{ij}(\boldsymbol{R}, \boldsymbol{z})$ is a component of of the $3N \times 3N$ EFT $\boldsymbol{\Lambda}$, where N is the number of atoms. Both these quantities are functions of the atomic positions $\boldsymbol{R} = (R_1, \ldots, R_N)$ and their corresponding atomic element types $\boldsymbol{z} = (z_1, \ldots, z_N)$. $F_i^{\mathcal{R}}(t)$ is a white noise force governed by electronic friction.

Maurer *et al.* [49] proposed an expression to evaluate $\boldsymbol{\Lambda}$ based on first-order TDPT within DFT,

$$\Lambda_{ij}(\hbar\omega) = \pi\hbar \sum_{\mathbf{k},\sigma,m,n} w_{\mathbf{k}} \tilde{g}^i_{mn}(\mathbf{k}) \left[\tilde{g}^j_{mn}\right]^*(\mathbf{k}) \times (f_{n\mathbf{k}} - f_{m\mathbf{k}}) \frac{\delta(\epsilon_{m\mathbf{k}} - \epsilon_{n\mathbf{k}} - \hbar\omega)}{\epsilon_{m\mathbf{k}} - \epsilon_{n\mathbf{k}}}, \quad (2)$$

where $w_{\mathbf{k}}$ are Brillouin zone sampling weights, $\tilde{g}^i_{mn}(\mathbf{k})$ are electron-phonon coupling (EPC) matrix elements describing nonadiabatic coupling between Kohn-Sham single-particle states m and n at wave vector $\mathbf{k}$, and σ is the spin label. The states have energies given by $\epsilon_{m\mathbf{k}}$ and occupations as

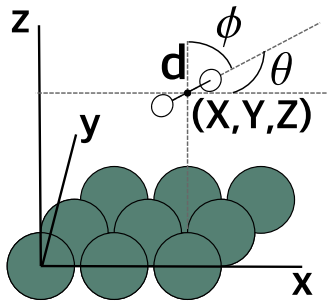

FIG. 1. Cartesian and internal coordinates for a diatomic molecule. The Cartesian coordinates (x, y, z) are presented along the internal counterparts (d, θ, ϕ, X, Y, Z) for H_2 molecule at Cu(111) surface, where d corresponds to an interatomic distance between H atoms, and θ and ϕ to polar and azimuthal angles with respect to the surface normal. X, Y, and Z represent the center-of-mass positions of the adsorbate molecule.

$f_{n\mathbf{k}}$. In typical calculations, the EFT is evaluated in the quasistatic limit ($\hbar\omega \to 0$). This formulation of the ODF method accounts for vibrational mode dependence and directional anisotropy of the EFT. Also commonly applied is a similar expression that is valid in the low-temperature limit (denoted $\mathbf{\Lambda}^0$) [15,51],

$$\Lambda^0_{ij} = \pi\hbar \sum_{\mathbf{k},\sigma,m,n} w_{\mathbf{k}} \tilde{g}^i_{mn}(\mathbf{k}) \left[\tilde{g}^j_{mn}\right]^*(\mathbf{k}) \delta(\epsilon_{n\mathbf{k}} - \epsilon_F)\delta(\epsilon_{m\mathbf{k}} - \epsilon_F), \tag{3}$$

with ϵ_F being the Fermi energy. This expression experiences problematic convergence behavior, attributed to the divergence of this expression at the Brillouin zone origin ($\mathbf{q} = 0$) [50,65]. Box *et al.* [50] examined the differences between Λ and Λ^0 formulations for H_2 on Cu(111), finding that Λ^0 yields systematically larger friction values and poorer numerical convergence. As a consequence, Λ^0 tends to overestimate vibrational lifetimes and phonon linewidths [65]. We therefore in this work employ 2 to evaluate the full ODF EFT.

The local-density friction approximation (LDFA) provides an efficient alternative to approximate $\mathbf{\Lambda}$ by assuming an adsorbate ion interacts with an isotropic, homogeneous electron gas characterized by the local electron density, ρ_{emb}, of the metal surface,

$$\Lambda^{\text{LDFA}}(\rho_{\text{emb}}) = \frac{4\pi\rho_{\text{emb}}}{k_F} \sum_{l=1}^{\infty} (l+1)\sin^2\left[\delta^F_l - \delta^F_{l+1}\right], \tag{4}$$

where k_F is the Fermi momentum, and δ^F_l is the scattering phase-shift at the Fermi level. Instead of calculating the full EFT, LDFA evaluates an isotropic coefficient that is applied identically along the Cartesian diagonal elements (Λ^{LDFA}). This approximation is highly efficient and significantly reduces computational complexity, but neglects the directional dependencies of the dissipation. In practical calculations, the tabulated phase shifts [66,67] are used, hence, the problem is reduced to evaluating the electron density of the surface metal at the position of the adsorbate atom.

The EFT can be represented within Cartesian (x, y, z) or internal (d, θ, ϕ, X, Y, Z) coordinates, as shown in Fig. 1. The coordinate transformation is explained in more detail within the Supplemental Material (SM) [68].

B. Machine learning representations

1. Atomic cluster expansion

The ACE [62] provides a framework to construct highly efficient MLIPs that achieve high body order representation.

In ACE, the atomic basis $A_{z_i,znlm}$ is defined as a projection of the neighborhood density ρ^z_i of all atoms of chemical element z around atom i (where atom i belongs to the chemical element z_i) onto the one-particle basis functions $\phi^{z_iz_j}_{nlm}$

$$A_{z_i,znlm} = \left\langle \rho^z_i \middle| \phi^{z_iz}_{nlm} \right\rangle = \sum_{\substack{j \\ \forall z_j = z}} \phi^{z_iz_j}_{nlm}(\boldsymbol{r}_{ij}), \tag{5}$$

where $\boldsymbol{r}_{ij} = R_j - R_i$ denotes the displacement of the atom j from the atom i, and the one-particle basis functions are summed over atoms j, for which $z_j = z$. The z_i, z_j are the respective element types z of central i and neighboring j atoms, and the density can be described as

$$\rho^z_i(\boldsymbol{r}) = \sum_{\substack{j\neq i \\ \forall z_j = z}} \delta(\boldsymbol{r} - \boldsymbol{r}_{ij}), \tag{6}$$

and the one-particle basis function can be defined as a product of a radial function $R^{z_iz_j}_{nl}$ and spherical harmonics Y^m_l,

$$\phi^{z_iz_j}_{nlm}(\boldsymbol{r}) = R^{z_iz_j}_{nl}(r) Y^m_l(\hat{\boldsymbol{r}}), \tag{7}$$

where $r = |\boldsymbol{r}|$ and $\hat{\boldsymbol{r}} = \boldsymbol{r}/r$. To obtain permutation-invariant basis functions, products of atomic basis functions are constructed

$$A_{z_i\boldsymbol{\upsilon}} = \prod_{t=1}^{\nu} A_{z_i\upsilon_t}, \tag{8}$$

where $\upsilon = znlm$, $\boldsymbol{\upsilon} = (\upsilon_1, \ldots, \upsilon_\nu)$ and ν refers to correlation order, corresponding to a (ν+1)-body basis function. Taking the products of atomic basis functions allows a convenient and efficient construction of basis functions of any body order. Isometry invariant basis $B_{z_i\eta_\nu}$ functions are created from the non-rotationally-invariant basis functions $A_{z_i\boldsymbol{\upsilon}}$,

$$B_{z_i\eta_\nu} = \sum_{\boldsymbol{\upsilon}} C_{\eta_\nu\boldsymbol{\upsilon}} A_{z_i\boldsymbol{\upsilon}}, \tag{9}$$

where $C_{\eta_\nu\boldsymbol{\upsilon}}$ are generalized Clebsch-Gordan coefficients, and all the allowed invariant contractions of $A_{z_i\boldsymbol{\upsilon}}$ are enumerated by η_ν. An interatomic potential model can be defined as a sum of site contributions,

$$E = \sum_i E_i = \sum_i \sum_{\eta_\nu} c_{z_i\eta_\nu} B_{z_i\eta_\nu}, \tag{10}$$

where $c_{z_i\eta_\nu}$ coefficients are free model parameters optimized in a linear-fitting procedure.

2. ACE-friction

Following the general approach for machine learning of friction tensors introduced in [61], we assume a representation

of the friction tensor as

$$\Lambda_{ij} = \sum_k \mathbf{\Sigma}_{ik}(\mathbf{\Sigma}_{jk})^T, \tag{11}$$

where each $\mathbf{\Sigma}_{ij}$ is a 3×3 matrix-valued function of atoms within a pair environment $\mathcal{N}(i, j)$ of the respective atom pair ij. That is, for $i \neq j$, the pair environment $\mathcal{N}(i, j)$ contains all atoms within a cutoff region that is rotationally symmetric around the displacement vector R_{ij} and for $i = j$, the environment $\mathcal{N}(i, j)$ reduces to the standard atomic site environment $\mathcal{N}(i)$ defined by a spherical cutoff region centered at R_i. Moreover, each $\mathbf{\Sigma}_{ij}$ is assumed to be matrix-equivariant with respect to the orthogonal group in dimension 3, $O(3)$, in the sense that

$$\forall Q \in O(3): \quad \mathbf{\Sigma}_{ij}(Q\boldsymbol{R}, z) = Q\mathbf{\Sigma}_{ij}(\boldsymbol{R}, z)Q^T,$$

and permutation-invariant with respect to permutations that leave the indices i, j of the respective atom pair unchanged, i.e.,

$$\forall \sigma \in S_N, \sigma i = i, \sigma j = j : \mathbf{\Sigma}_{ij}(\sigma\boldsymbol{R}, \sigma z) = \mathbf{\Sigma}_{ij}(\boldsymbol{R}, z),$$

where S_N denotes the symmetric group of degree N. The action of a permutation $\sigma \in S_N$ on the position vector $\boldsymbol{R}$, and atomic element vector z, is $\sigma\boldsymbol{R} = (R_{\sigma 1}, \ldots, R_{\sigma N})$ and $\sigma z = (z_{\sigma 1}, \ldots, z_{\sigma N})$, respectively.

The representation (11) of the friction tensors is referred to in [61] as a *rowwise coupling* ansatz. As detailed in [61], this ansatz is one of several that, together with the stated equivariance properties of the matrix blocks $\mathbf{\Sigma}_{ij}$, guarantee that the resulting friction tensor $\mathbf{\Lambda}$ is symmetric positive semidefinite and satisfies the correct equivariance relation with respect to relevant isometric transformations in configurational space, which are

$$\begin{aligned} \forall Q \in O(3): &\quad \mathbf{\Lambda}_{ij}(Q\boldsymbol{R}, z) = Q\mathbf{\Lambda}_{ij}(\boldsymbol{R}, z)Q^T, \\ \forall \sigma \in S_N: &\quad \mathbf{\Lambda}_{ij}(\sigma\boldsymbol{R}, \sigma z) = \mathbf{\Lambda}_{\sigma i \sigma j}(\boldsymbol{R}, z). \end{aligned}$$

To expand blocks $\mathbf{\Sigma}_{ij}$ in an ACE basis, we assume these to be of the functional form

$$\mathbf{\Sigma}_{ij} = \mathcal{M}^{z_i}_{\text{on}}(\{(\boldsymbol{r}_{ik}, z_k)\}_{k\in\mathcal{N}(i)}),$$

if $i = j$, and

$$\mathbf{\Sigma}_{ij} = \mathcal{M}^{z_i z_j}_{\text{off}}\left(\boldsymbol{r}_{ij}, \left\{\left(\boldsymbol{r}^{\lambda}_{ijk}, z_k\right)\right\}_{k\in\mathcal{N}(i,j)}\right),$$

for $i \neq j$, where $\boldsymbol{r}^{\lambda}_{ijk} := R_k - (\lambda R_i + (1-\lambda)R_j)$ for some prescribed $\lambda \in [0, 1]$. Here, a set notation is used to indicate that the functions $\mathcal{M}^{z_i}_{\text{on}}$ and $\mathcal{M}^{z_i z_j}_{\text{off}}$ are invariant under permutation of the order of the arguments contained in the respective multisets.

The functions $\mathcal{M}^{z_i}_{\text{on}}$ can be linearly expanded as

$$\mathcal{M}^{z_i}_{\text{on}} = \sum_{\eta_v} c_{z_i,\eta_v} B^{(2)}_{z_i,\eta_v}, \tag{12}$$

using a matrix-equivariant ACE basis $(B^{(2)}_{z_i,\eta_v})_{\eta_v}$ and coefficients $c_{\eta_v} \in \mathbb{R}$. This matrix-equivariant ACE basis is constructed from the atomic basis functions as

$$B^{(2)}_{z_i,\eta_v} = \sum_{\boldsymbol{v}} C^{(2)}_{\eta_v \boldsymbol{v}} A_{z_i,\boldsymbol{v}}, \tag{13}$$

using matrix-valued coupling coefficients $C^{(2)}_{\eta_v \boldsymbol{v}} \in \mathbb{R}^{3\times 3}$ that are such that each $B^{(2)}_{z_i,\eta_v}$ satisfies the same equivariance symmetry with respect to $O(3)$ as $\mathbf{\Sigma}_{ij}$ (and $\mathcal{M}^{z_i}_{\text{on}}$), i.e.,

$$\begin{aligned} \forall Q \in O(3): &\quad B^{(2)}_{z_i,\eta_v}(\{(Q\boldsymbol{r}_{ik}, Z_k)\}_{k\in\mathcal{N}(i)}) \\ &= QB^{(2)}_{z_i,\eta_v}(\{(\boldsymbol{r}_{ik}, Z_k)\}_{k\in\mathcal{N}(i)})Q^T. \end{aligned}$$

An ACE basis expansion of the function $\mathcal{M}^{z_i z_j}_{\text{off}}$ can be constructed as a modification of the basis $(B^{(2)}_{z_i,\eta_v})_{\eta_v}$; see [61,69] for more details.

To learn a friction tensor from data, a finite subset of ACE basis functions used in the expansion of $\mathcal{M}^{z_i}_{\text{on}}$ and $\mathcal{M}^{z_i z_j}_{\text{off}}$ is selected and the corresponding coefficients are fitted by minimizing a non-linear loss function that penalizes discrepancy (measured in terms of a prescribed matrix norm) between evaluations of the resulting parametric model of the friction tensor and evaluations of the EFT obtained from electronic structure calculations.

C. Computational details

1. Potential energy surface

We employ MACE-based [70] MLIP models from Ref. [59], trained using a database from Ref. [58]. The database included 4230 structures, with 1685 Cu-only surface structures sampled at different temperatures (300 K, 600 K, and 900 K), and 2545 H_2/Cu structures. The database contains structures including four Cu facets, namely Cu(111), (100), (110), and (211). 3×3, six-layered slabs for all the surfaces in the database were used with the exception of the Cu(211) surface, for which 1×3, six-layered slabs were used. The database was built with adaptive sampling, during which structures that are not well represented by the current iteration of the models are selected, labels are generated with DFT, and data points are added to the database. The models are retrained with the updated database. This was repeated four times until the final dynamical observable matched the reference values. More details about the database preparation can be found in Ref. [58].

For DFT energy and force calculations, a specific reaction parameter (SRP) functional [71] containing 52% of PBE [72] and 48% of RPBE functional [73] (SRP48) was used with a k-grid of $12 \times 12 \times 1$ and a tight basis set within the FHI-aims [74] all-electron electronic structure code. Minimum energy paths were obtained using the CI-NEB method [75], at DFT- and MLIP-level, as detailed in Ref. [59]. The two bottom layers of Cu atoms were frozen during optimizations.

2. LDFA training data generation

LDFA models are based on an ML model that predicts the clean metal surface density $\rho_{\text{emb}}(\mathbf{R})$ at any given point as a function of the position of the clean surface atoms. This model is used to evaluate the electronic friction coefficient for each H atom independently, from which the LDFA EFT is then constructed. The separate treatment of each H atom is possible due to the isotropic nature of LDFA. We evaluate the Wigner-Seitz radius $r_s(\rho_{\text{emb}})$,

$$r_s(\rho_{\text{emb}}) = \left(\frac{3}{4\pi\,\rho_{\text{emb}}}\right)^{1/3} \tag{14}$$

and use an interpolation function (cubic spline) to fit the tabulated LDFA friction coefficients as provided by Gerrits *et al.* [67].

To build the density model, a dataset is constructed that contains the density values for certain coordinates within the unit cell at different surface configurations. The clean metal surface electronic densities were extracted from densely sampled cube files using the FHI-aims [74] electronic structure code, employing "tight" settings for basis sets. In total, 200 cube files were generated (50 surface configurations per surface facet). The cube files were evaluated for surfaces equilibrated at three different temperatures, 300, 600, and 900 K. From each cube file, roughly 30 density values were selected at random positions within the unit cell between the first sublayer and 7 Å above the surface. The densities were read at least 0.8 Å away from any Cu atom, to avoid high-density peaks close to atom centers that could cause issues in ML model training. The value of 0.8 Å was chosen as the minimal distance that can occur between H and Cu atoms at the collision energies of 0.1–1.0 eV. This distance was chosen based on previous scattering simulations. Overall, 6000 data points were used in the final dataset (4800 in the training dataset, and 1200 in the test set), each containing coordinates of a single H atom and Cu surface atoms, and the corresponding background electronic density of Cu surface atoms at the H atom position. See Fig. S1 within the SM [68] for a visualization of the constructed dataset for Cu(111).

The density models were trained using ACEpotentials.jl [76,78]. The energies used for the training of ACEpotentials.jl models were replaced with densities, thus, no energies or forces were used in the training of the models. A solver based on Bayesian linear regression (BLR) is used for all the models, within `ace_basis` interface. In the final model, a correlation order of 3 was used with the corresponding maximum polynomial degrees of 12, 10, and 10, and with a cutoff distance of 4 Å. More information about the optimization of model parameters and the final parameters used for the models can be found in Sec. III A 1.

3. ODF training data generation

The dataset for the ODF-based EFT model was constructed by taking a subset of structures from the dataset collected for the MACE PES described in our previous publication [58], excluding the structures that contain bare metal surface (1685 structures), and including only the random subset of H_2/Cu structures (1602 out of 2545). For the Cu(211) surface, a larger slab was required to converge the EFT than was used for the energy and force evaluation (1×4 instead of 1×3). We, therefore, replaced the data points corresponding to this surface (261 structures) with structures generated by sampling new scattering dynamics trajectories (382 structures), which were evaluated using the MACE PES. The sampled trajectories were initialized with different H_2 translational energies, ranging from 0.2 eV to 0.9 eV, and with surface temperatures of 300, 600, and 900 K. The sampling included a clustering procedure using the k-means method. ODF-based EFT was calculated for the prepared set of structures, using Eq. (2) with a Gaussian broadening width of 0.4 eV as a replacement for the delta function, and a Fermi factor corresponding to an electronic temperature of 300 K. The electronic friction calculations did not require a "tight" basis set as needed for PES, and thus "light" settings with additional "second tier" basis functions for hydrogen (within FHI-aims) were sufficient for the evaluation of ODF-based EFT. Details of the convergence tests are provided within the SM [68].

The ODF-based electronic friction models (ACE-friction) were trained using ACEds.jl code (version 0.1.7) [77], currently maintained within the ACEfriction.jl package [61,79]. The ODF calculations were done within the atom-centered scheme (employing columnwise couplings), utilizing L2 regularization with Adam optimizer, for which a learning rate of 10^{-4} was used together with exponential decay rate for the momentum and velocity terms of 0.99, and 0.999, respectively. In the final model, a maximum correlation order of 2 was used with the corresponding maximum polynomial degree of 6, and with the cutoff distance of 5 Å. More information about the optimization of model parameters and the final parameters used for the models can be found in Sec. III A 2.

4. Simulation details

All MD simulations and preparation of initial conditions were performed using the NQCDynamics (version 0.13.4) [80,81]. All the trajectories in this study include H_2 scattering dynamics at different Cu surfaces and are initiated with a hydrogen molecule placed 7 Å above the surface. Initial conditions for H_2 are generated using the Einstein-Brillouin-Keller (EBK) method [82] for different normal incidence energies (initial incidence angle of H_2 $\phi = 0°$) and rovibrational states with randomly chosen azimuthal and polar angles. The two bottom metal layers were frozen in all simulations. Simulations at 0 K surface temperatures were initiated using a DFT-relaxed slab with initial velocities based on the Maxwell-Boltzmann distribution. Simulations at finite temperatures were initialized with surface positions obtained from a random sampling of surface-only Langevin MD output structures at the selected temperatures. Lattice expansion is accounted for based on the relation between lattice constant and surface temperature, as described in Ref. [59]. To ensure that the statistical errors are negligible, sticking, survival, and transition probabilities were calculated using data averaged over 20,000 trajectories for every model, surface facet, rovibrational state, and collision energy reported in this study. More details on statistical errors can be found within the SM [68]. The maximum simulation time of every trajectory was 3 ps with a time step of 0.1 fs unless special conditions were met, such as the distance between hydrogen atoms at the metal surface being above 2.25 Å or the distance between the hydrogen molecule and top surface atoms being above 7.2 Å. State-to-state survival and transition probabilities are evaluated by dividing the number of trajectories that end with the desired final rovibrational state of H_2 over all the trajectories, including the ones that led to dissociation. The details on the evaluation of dynamical observables described in this study are included in the SM [68].

III. RESULTS AND DISCUSSION

A. Validation of electronic friction representations

In the following sections, we describe nonadiabatic effects within MDEF with two configuration-dependent ML surrogate models of the EFT for LDF and ODF as described in Sec. II. Further details of the data generation and model construction are reported in the SM [68]. Below, we present the details of hyperparameter optimization and validation of models based on evaluation errors, as well as their performance on the dynamical simulations.

1. LDFA model

The optimization (cross-validation) of model parameters was performed for density models based on ACEpotentials.jl code [78]. In Fig. S2 within the SM [68], the model size (correlation order and corresponding polynomial degrees) and cutoff distance are plotted against the root mean squared errors (RMSEs). Additionally, density evaluation times obtained for the corresponding models are included. ACE-based density models achieve rapid convergence with respect to both model size and cutoff distance, resulting in low evaluation times of roughly 15 ms (per single H at the Cu surface). Even considering the separate evaluations for each H atom, this is almost two times faster than the force evaluation with our MACE PES model (roughly 50 ms). The model RMSE converges already for correlation order (N) of 2 with higher polynomial degrees (10 and 6 or 16 and 2). Full convergence is already achieved with a cutoff distance of 3 Å. In the final density model, the correlation order of 3 is used with the corresponding polynomial degrees (for each order) of 12, 10, and 8, respectively. In the final model, a cutoff distance of 4 Å was used.

Aside from several outliers corresponding to the Cu(111) surface, the ACE predicted density values match the reference densities across the entire spectrum of the densities in the test set as shown in Fig. S3 within the SM [68]. The maximum difference from the reference is 0.05 $Å^{-3}$. The final RMSE and mean absolute error (MAE) are 0.004 $Å^{-3}$ and 0.002 $Å^{-3}$.

The final predicted LDFA values show excellent agreement with DFT values along simulated dissociation trajectories (Fig. 2) for the four different copper surfaces, namely, Cu(111), Cu(100), Cu(110), and Cu(211). The shown trajectories were chosen randomly from the trajectories run with MACE PES. The LDFA-based electronic friction along the diagonal elements generally increases as the molecule approaches the surface across all considered copper facets. Notably, for Cu(110), the friction exhibits a distinct drop just before dissociation, whereas for Cu(211) and Cu(100), the friction peaks prior to dissociation. After dissociation, the electronic friction reaches its highest values for hydrogen atoms on the Cu(111) surface. The friction for dissociated hydrogen atoms is approximately 0.4 meV ps $Å^{-2}$ for Cu(100), Cu(110) and Cu(211), while for Cu(111), it is slightly elevated at around 0.47 meV ps $Å^{-2}$. A similar comparison is shown in Fig. S4 within the SM [68] for scattering trajectories, where the excellent agreement between LDFA based on ACE and DFT holds across all facets.

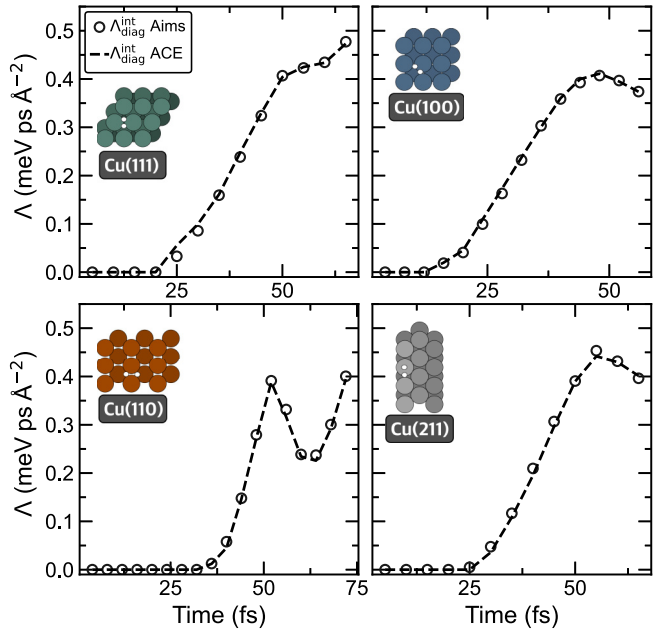

FIG. 2. Predictions of LDFA-based EFT elements along the trajectories of H_2 dissociation on Cu surfaces. The diagonal elements of EFT (internal coordinates) are plotted for dissociation trajectories at Cu surfaces, predicted by the ACE model, and compared to reference values calculated using FHI-aims. Note that all the diagonal components of the EFT are identical in normalized internal coordinates. Criteria to identify dissociation are given in Sec. II.

2. ODF model

The convergence of the DFT calculations of the ODF EFT has been carefully studied. We find that the dd element convergence is slower than for the ZZ element with respect to k-grid size as shown (Fig. S5 within the SM [68]). However, the convergence of all the considered surfaces is consistent, and a satisfactory level of convergence (±10% variation in the EFT values) is reached around $N_k = 12$ for both investigated elements. A Gaussian broadening width of 0.4 eV was chosen to evaluate ODF, as this is a compromise between achieving stable EFT prediction and excessive broadening across the surface facets (Fig. S6 within the SM [68]). In most previous studies, the broadening widths of 0.6 were chosen [15,46]. Large broadening widths can lead to the incorporation of non-zero frequency contributions that are not included in the first-order approximation within many-body perturbation theory. Our results are relatively insensitive to the choice of broadening within the range of 0.3–0.8 eV. A "light" basis is employed, as defined in FHI-aims, as ODF coefficients were already converged with this choice of basis set.

A 3 × 3 unit cell was chosen for the calculations involving Cu(111), Cu(110), and Cu(100) surfaces, and 1 × 4 unit cell for the Cu(211) surface, with 6 layers for all surfaces, as these gave stable ODF coefficient predictions (Fig. S7 within the SM [68]).

A cross-validation optimization of the ODF ACE-friction model parameters was performed, in which an 80%/20% train/test split was used. Different settings were tested for maximum correlation order and maximum polynomial degree (Fig. S8 within the SM [68]).

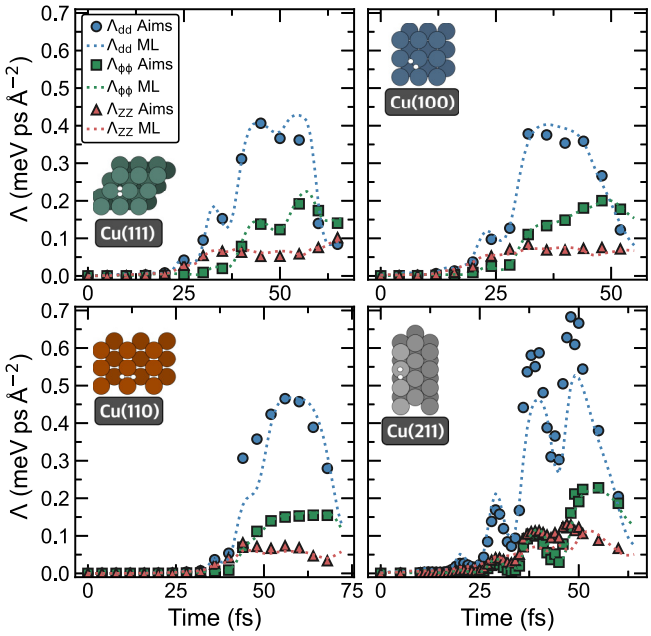

FIG. 3. Predictions of ODF-based EFT elements across trajectory steps of H_2 dissociation on Cu surfaces. Electronic friction values (internal coordinates) are plotted for dissociation trajectories (the same as in Fig. 2) at Cu surfaces predicted by the ACE-friction model and compared to reference values calculated using FHI-aims. Dissociation criteria are given in Sec. II.

ODF models were trained with maximum correlation orders from 1 to 3 (left side of Fig. S8). RMSEs improved up to order 2, with no further gains at higher orders. Since higher orders significantly increase evaluation time, order 2 was chosen for the final models. ODF models were trained with maximum polynomial degrees from 2 to 10 for a correlation order of 2 (right side of Fig. S8 within the SM [68]). A degree of 6 was found to be optimal, with higher degrees reducing training RMSEs but increasing test RMSEs, likely due to overfitting. The EFT evaluation time for the ODF ACE-friction model is 40 ms, only slightly slower than the LDFA-based EFT(30 ms), but it computes the full EFT rather than just two diagonal values. Additionally, RMSEs were tested for cutoff distances from 3 to 7 Å (Fig. S9 within the SM [68]). RMSEs improve rapidly between 3 and 4 Å, with only slight improvement up to 5 Å. Beyond this, RMSEs increase, likely caused by cutoff overlap between periodic unit cells. A 5 Å cutoff was chosen for the final models. The model performance is shown in Fig. S10 within the SM [68], comparing ACE-friction predictions with DFT reference values. The predictions align well with the reference data (MAE of 0.0038 meV ps $Å^{-2}$ and RMSE of 0.0083 meV ps $Å^{-2}$), with some outliers for higher electronic friction values.

To assess the accuracy of the final ACE-friction model, EFT was evaluated along scattering (Fig. S11 within the SM [68]) and dissociation (Fig. 3) trajectories using both the ACE-friction model and the reference DFT data. This evaluation covered all four Cu surfaces in this study. Three electronic friction components in the internal coordinate system were compared: internal stretch of the adsorbate atoms (d), azimuthal angle (ϕ), and the center of mass in the z direction (Z) (see SM [68] for details on the coordinate transformation). The ACE-friction model predictions generally agree well with the reference values (Aims). However, notable discrepancies appear in some cases, such as $\Lambda_{\phi\phi}$ in H_2 scattering on Cu(110) and Λ_{dd} in H_2 dissociation on Cu(211). This behavior persists in models retrained with different settings (e.g., with a maximum correlation order of 3). Similar to the LDFA case, the electronic friction increases on approach to the surface, however, the final dissociation product states exhibit significantly lower electronic friction values (maximum of 0.15 meV ps $Å^{-2}$) than the corresponding LDFA values, which exceed 0.35 meV ps $Å^{-2}$ across all surfaces. In some cases, particularly near the dissociation barrier where the EFT values peak, the ACE-friction model deviates more significantly from the reference data. These deviations likely do not translate into large errors in friction forces as they occur in the transition state regions where velocities are low (see Figs. S16 and S17 within the SM [68]). As per Eq. (1), the corresponding effect on the friction forces will be small.

3. *Electronic friction along minimum energy paths*

We evaluated electronic friction along the minimum energy paths for H_2 dissociative chemisorption on Cu(111), Cu(100), Cu(110), and Cu(211) surfaces using reference FHI-aims ODF calculations, as well as our ODF and LDFA models (Fig. 4). The ODF ML model closely follows the reference electronic friction values, which for all surface facets exhibit an increase in EFT elements to the transition state, and then a decrease to the dissociated product state with few exceptions, such as the ZZ element for Cu(211). The LDFA model produces isotropic friction values, resulting in identical internal EFT elements when using a unitary coordinate transformation. While LDFA values around the transition state align with the Λ_{dd} ODF values (approximately 0.4 meV ps $Å^{-2}$), they increase further for the final dissociation structure. This contrasts with the ODF values, which decrease to near 0.1 meV ps $Å^{-2}$ in the final structure. As discussed in Ref. [52] for H/Pt(111), LDFA significantly overestimates electronic friction for chemisorbed hydrogen atoms on metal surfaces, resulting in much shorter vibrational lifetimes than observed experimentally. The discrepancy between LDFA and ODF for the chemisorbed state is consistent across all studied copper facets. Previous ODF results [15,45,83] for H_2/Cu(111) used Λ^0, which showed a smaller disparity between LDFA and ODF in the product state [50]. Figure S13 within the SM [68] shows a comparison of our EFT values along H_2/Cu(111) dissociation minimum energy path with previous works [15,45,83].

B. Validation against experiment

We now turn to benchmarking our simulations against experimental measurements and prior theoretical studies. These comparisons allow us to critically assess the accuracy and transferability of the MLIP and EFT ML models across observables and to evaluate the impact of electronic friction on inelastic energy redistribution during state-to-state scattering. While recent work has shown that adiabatic BOMD simulations based on our MLIP yield good agreement with experimental sticking probabilities on Cu(111) and Cu(211)

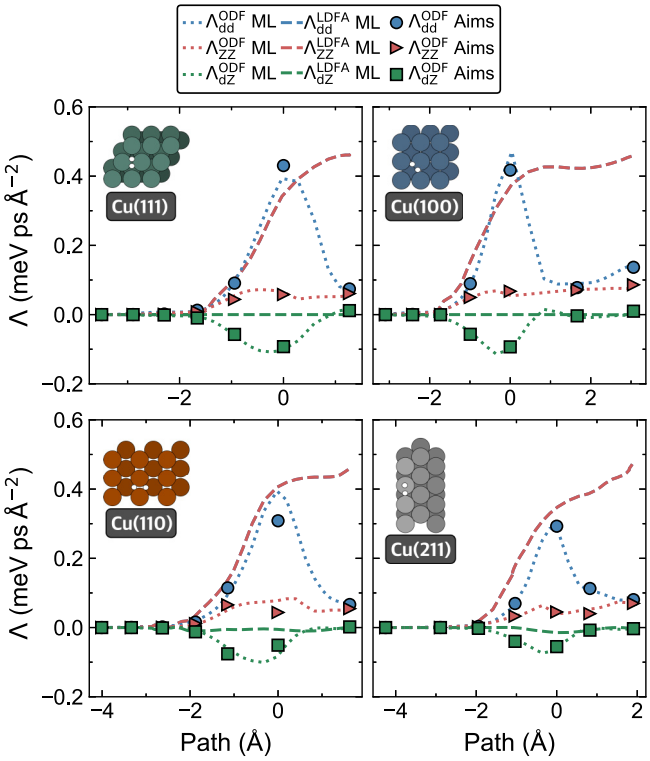

FIG. 4. Electronic friction values along minimum energy paths of dissociative adsorption of H_2 at Cu surfaces. EFT elements (Λ_{dd}, Λ_{dZ}, and Λ_{ZZ}) are shown for different Cu surfaces along the minimum energy paths, evaluated with FHI-aims (ODF), and two ML-based models, based on LDFA (dashed lines) and ODF methods (solid lines). The transition state along the path in each case is located at 0 Å. Friction values are shown in the internal coordinate system (Fig. 1), where d corresponds to an interatomic distance between H atoms, and θ and ϕ to polar and azimuthal angles with respect to the surface normal. X, Y, and Z represent the center-of-mass positions of the adsorbate molecule.

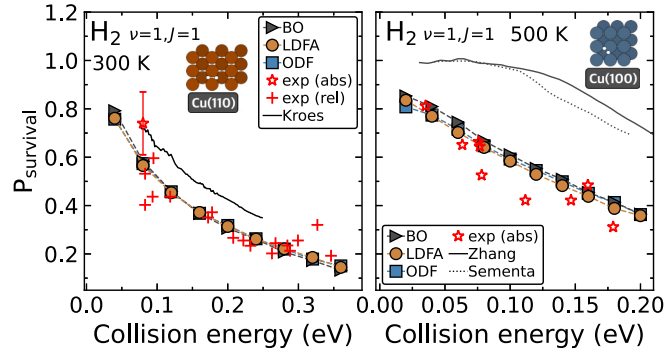

FIG. 5. Survival probabilities for the state-to-state scattering of H_2 at Cu(110) and Cu(100) surfaces. Survival probabilities of H_2 ($\nu = 1, J = 1$) at Cu(110) and Cu(100) surfaces are plotted for a set of translational energies (in eV) (at 300 K and 500 K, respectively) and compared with previous computational and experimental results. The probabilities were calculated using classical BOMD (triangles), MDEF-LDFA (circles), and MDEF-ODF (squares). Survival probabilities for H_2 scattering at Cu(110) are compared with theoretical results by Kroes *et al.* [84] (solid-black line) and relative experimental survival probabilities by Gostein *et al.* [85] scaled such that the highest collision energy matches our simulations (red crosses). A single available absolute experimental probability by Gostein *et al.* [86] is also included with a corresponding error bar (red star). For H_2 scattering at Cu(100), the survival probabilities are compared with absolute (nonscaled) experimental survival probabilities by Watts *et al.* [20] (red stars), and theoretical results by Zhang *et al.* [87] (solid-black line) and Sementa *et al.* [88] (dotted-black line).

[59], we now focus on the quantum state distribution of scattered molecules where the role of nonadiabatic effects may be more significant.

Rovibrational state survival probabilities for H_2 ($\nu = 1$, $J = 1$) scattering on the Cu(110) at 300 K were compared with experimental results (single absolute survival probability data point and set of relative probabilities) by Gostein *et al.* [85,86] and theoretical predictions by Kroes *et al.* [84]. The latter results are based on time-dependent quantum wavepacket dynamics based on the PW91 functional and a static surface approximation (Fig. 5, left).

All methods and experiments show a decrease in survival probabilities with increasing collision energy. Absolute survival probabilities by Kroes *et al.* [84] are consistently about 0.1 larger than our BOMD, MDEF-LDFA, and MDEF-ODF results across all energies. However, the results of Kroes *et al.* capture the relative decrease in survival probability as well as our results. The absolute offset in survival probability may stem from their use of the PW91 functional, whereas we employed SRP48. Another factor could be our inclusion of surface movement at 300 K, in contrast to the rigid surface model used by Kroes *et al.* [84]. The incorporation of electronic friction shows a negligible effect when compared to BOMD, suggesting that nonadiabatic effects have little impact on the rovibrational survival probability of H_2 ($\nu = 1, J = 1$) in scattering at Cu(110). Only a single absolute survival probability is available from experiments, and due to a relatively large error (0.13), we cannot make a firm judgment on which theoretical curve gives a more accurate prediction.

All our models agree well with absolute survival probabilities for H_2($\nu = 1$, $J = 1$) elastic scattering at Cu(100) surface at 500 K, measured by Watts *et al.* [20], across all studied collision energies (Fig. 5, right). This is a significant improvement over previous results by Sementa *et al.* [88] using an adiabatic approach, employing a PES based on the SRP43 functional (43% RPBE, 57% PW91) and Zhang *et al.* [87] using a quantum-dynamical approach employing a time-dependent wave packet method with a different transferable MLIP [57] based on the optPBE-vdW functional [89]. Both the reference theoretical results use rigid metal surfaces in their simulations and made similar predictions of survival probabilities, however, both significantly overestimated the survival probabilities compared to the experiment. Such improvement in accuracy could be attributed to either the inclusion of surface movement in the dynamics, which will have a significant effect at the experimental temperature of 500 K, or by the difference in exchange-correlation functional used. The negligible difference with or without friction again suggests that nonadiabatic effects are not significant for survival probabilities. However, an important benefit of the combined MLIP and EFT ML models is that we do not need to

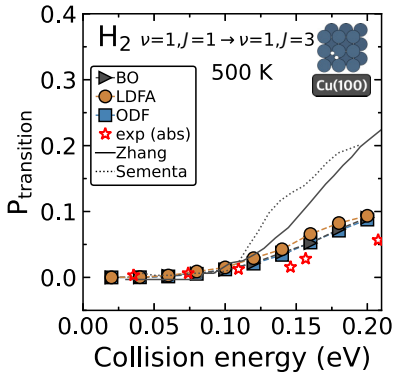

FIG. 6. Rotational excitation probabilities for the state-to-state scattering of H_2 at Cu(100) surface (500 K). The H_2 ($\nu = 1, J = 1 \rightarrow \nu = 1, J = 3$) probabilities were evaluated at different collision energies employing three different schemes, adiabatic (BOMD) (black triangles), MDEF with LDFA (orange circles), and MDEF with ODF (blue squares), using MACE-based PES, ACE density model (LDFA), and ACE-friction model (ODF). The H_2 ($\nu = 1, J = 1 \rightarrow \nu = 1, J = 3$) transition probabilities are also compared with absolute (nonscaled) experimental survival probabilities by Watts *et al.* [20] (red stars) and theoretical results by Zhang *et al.* [87] (solid-black line) and Sementa *et al.* [88] (dotted-black line).

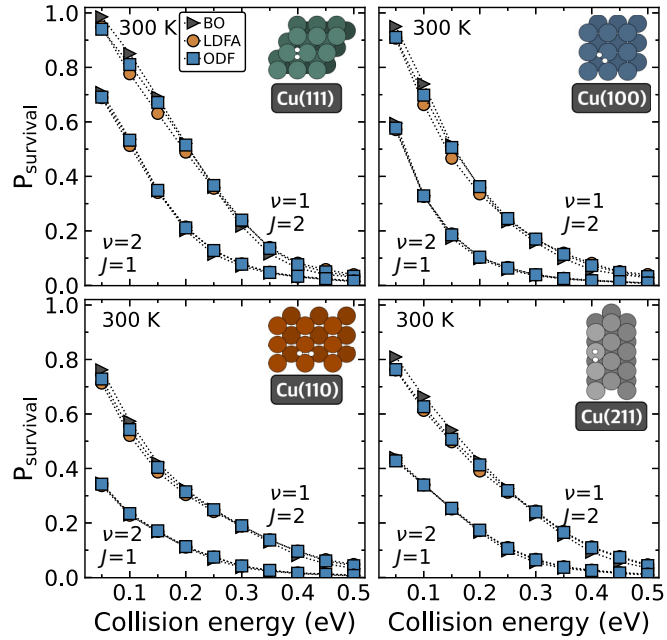

FIG. 7. Survival probabilities for the state-to-state scattering of H_2 at Cu surfaces. Survival probabilities of H_2 ($\nu = 1, J = 2$ and $\nu = 2, J = 1$) at Cu surfaces are plotted for a set of translational energies (eV) at 300 K. The probabilities were calculated using classical BOMD (triangles), MDEF-LDFA (circles), and MDEF-ODF (squares).

make a prior judgment whether to include nonadiabatic effects in our simulations or not.

In the same experimental work by Watts *et al.* [20], experimental $H_2(\nu = 1, J = 1 \rightarrow \nu = 1, J = 3)$ absolute rotational excitation probabilities were collected for scattering dynamics at Cu(100) at 500 K. In Fig. 6, simulated transition probabilities for rotational excitation of H_2 ($\nu = 1, J = 1 \rightarrow \nu = 1, J = 3$) at Cu(100) at 500 K are compared with experimental results by Watts *et al.* [20] and theoretical results by Zhang *et al.* [87] and Sementa *et al.* [88]. Close agreement with experimental results is obtained with the BOMD method, and no further improvement is visible when nonadiabatic effects are considered in the dynamics (using MDEF with either LDFA or ODF EFT representations). Such close agreement was not achieved by previous theoretical results that deviated from the experiment for collision energies above 0.1 eV. At the collision energy of 0.2 eV, the previous theoretical works predict transition probabilities of about 0.22, overestimating the probabilities by a factor of four compared to the experimental results.

Based on our validation results, we can conclude that the combination of the MACE MLIP developed by Stark *et al.* [59] and the EFT ML models presented here, represent the to-date most accurate models to simulate reactive surface chemistry of hydrogen on low-index facets of copper.

C. Dissociative chemisorption and rovibrationally elastic scattering across surfaces

Having established that the model is capable of simulating several phenomena correctly across different surface facets, we investigate how the surface morphology influences H_2 dissociation and scattering. To do so, we evaluate survival and sticking probabilities across four low-index Cu surfaces—Cu(111), Cu(100), Cu(110), and Cu(211)—using both adiabatic and nonadiabatic MD simulations (Figs. 7 and 8). Two initial rovibrational states were considered: ($\nu = 1$, $J = 2$) and ($\nu = 2$, $J = 1$). For all surfaces and methods, survival probabilities monotonically decrease with increasing collision energy, while sticking probabilities increase, consistent with barrier-limited dynamics.

The inclusion of electronic friction (LDFA and ODF) introduces only minor changes across the full energy range, indicating that these processes are predominantly adiabatic under the conditions studied. Differences between friction models are negligible, and trends in sticking and survival probabilities are robust against the choice of the method of evaluating the EFT.

Across all investigated surfaces, H_2 in the $\nu = 1$ vibrational state exhibits negligible sticking at the lowest collision energies. As energy increases, sticking rises first on Cu(110) and Cu(211), reflecting their greater reactivity at low incidence energies, while Cu(100) and Cu(111) show a delayed but sharper increase at higher energies. When the molecule is initially in the $\nu = 2, J = 1$ state, vibrational excitation significantly enhances reactivity on Cu(110) and Cu(211), resulting in appreciable sticking even at low translational energies. In contrast, Cu(100) and Cu(111) remain relatively inert at these energies, with sticking rising more steeply only at higher collision energies. These trends highlight the role of vibrational promotion, particularly on Cu(110) and Cu(211) surfaces.

Experimental measurements by Anger *et al.* [25] using molecular beam techniques report initial sticking coefficients for H_2 on Cu(111), Cu(100), and Cu(110) across a similar energy range. While these measurements do not resolve rovibrational states, they indicate a sticking order of Cu(111) >

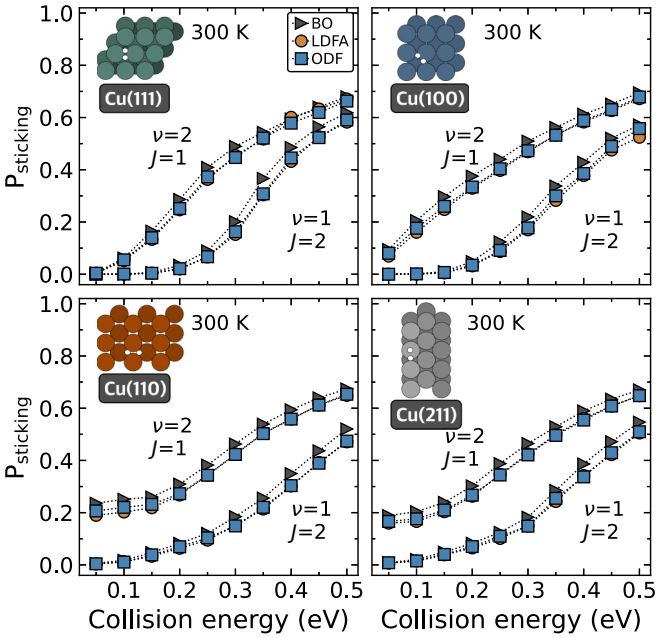

FIG. 8. Sticking probabilities evaluated at 300 K for H_2 dissociation on different Cu surfaces. The probabilities were evaluated at different collision energies employing three different schemes, adiabatic (BO), MDEF-LDFA, and MDEF-ODF, using MACE-based PES, ACE density model (LDFA), and ACE-friction model (ODF). The results were obtained for two H_2 rovibrational initial states, ($\nu = 2, J = 1$) and ($\nu = 1, J = 2$).

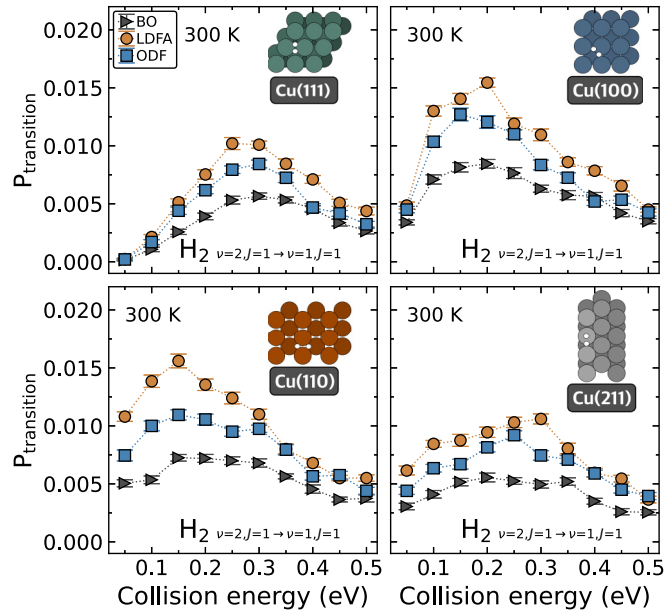

FIG. 9. Vibrational de-excitation probabilities for the state-to-state scattering of H_2 at Cu surfaces (300 K). Vibrational de-excitation of $H_2(\nu = 2, J = 1 \rightarrow \nu = 1, J = 1)$ at Cu(111), Cu(100), Cu(110), and Cu(211) surfaces are plotted for a set of translational energies (eV) at 300 K. The probabilities were calculated using classical BOMD (triangles), MDEF-LDFA (circles), and MDEF-ODF (squares). Statistical error bars shown, see SM [68] for details.

Cu(100) > Cu(110), which contrasts with our results for $\nu = 2$, $J = 1$ but more closely resembles our $\nu = 1$, $J = 2$ results. This suggests that the experimental measurements may reflect behavior closer to the vibrational ground state ($\nu = 0$), where vibrational promotion is absent or less pronounced.

To rationalize these trends, we examine the computed dissociation barriers E_{ads} and vibrational promotion energies $\Delta E_{\nu=2\rightarrow\nu=1}$ (Table I). Cu(110) exhibits the highest barrier (0.63 eV) and the strongest vibrational enhancement (0.18 eV), followed by Cu(100). Cu(111) has the next highest barrier (although not necessarily distinguishable within the computational uncertainty), but the weakest vibrational promotion. Despite its high barrier, Cu(110) shows high reactivity at low collision energy for $\nu = 2$, suggesting that geometrical effects and vibrational promotion facilitate access to the transition state.

These observations are consistent with the shape of the elbow plots (2D slices of the PES around the transition state): Cu(111) presents an early barrier, while Cu(110) and Cu(100) exhibit mid-barrier character, and Cu(211) shows a later transition state that is where vibrational promotion will be more beneficial (Fig. S14 within the SM [68]). This aligns with Polanyi-type behavior, where the location of the transition state dictates the effectiveness of vibrational excitation in promoting dissociation. For example, Cu(111) shows a stronger increase in sticking in response to increasing collision energy than Cu(110) and Cu(211).

TABLE I. Reaction barriers E_{ads} associated with dissociative chemisorption of H_2 at different Cu surfaces. The reaction barriers obtained for H_2 dissociation at Cu(111), Cu(100), Cu(110), and Cu(211) are listed, based on the CI-NEB calculations. Corresponding values from literature—labeled as E_{ads}[lit]—with the closest settings to our calculations are given for comparison's sake, too. Additionally, vibrational promotion energies ($\Delta E_{\nu=2\rightarrow\nu=1}$) are listed, which describe the difference in energy between the same sticking probability (0.3) at two different vibrational states $\nu = 1$ and $\nu = 2$. The DFT calculations were performed with the FHI-aims code, employing the SRP48 functional.

Surface	Cu(111)	Cu(100)	Cu(110)	Cu(211)
E_{ads} [this work] (eV)	0.56	0.58	0.63	0.52
E_{ads} [lit] (eV)	0.64[a]	0.67[b]	0.81[b]	0.64[c]
$\Delta E_{\nu=2\rightarrow\nu=1}$ (eV)	0.13	0.17	0.18	0.15

[a]xc = SRP48; $p(3 \times 3)$ cell; Static surface (taken from Ref. [90]).
[b]xc = optPBE-vdW; $p(2 \times 2)$ cell; Moving surface (taken from Ref. [57]).
[c]xc = SRP48; $p(3 \times 3)$ cell; Static surface (taken from Ref. [24]).

D. Rovibrationally inelastic scattering across surfaces

We next examined vibrational energy loss in rovibrationally inelastic scattering (Fig. 9), focusing on the transition $\nu = 2$, $J = 1 \rightarrow \nu = 1$, $J = 1$ at 300 K across all Cu surfaces. Vibrationally inelastic transition probabilities are low and weakly dependent on the incidence energy under adiabatic dynamics, but increase with a shift in peak position with the inclusion of nonadiabatic effects.

For all surfaces, nonadiabatic dynamics (LDFA and ODF) yield a higher dependence on the collision energy than adiabatic dynamics. The two schemes do not differ strongly from each other except in the case of the Cu(110), where LDFA predicts higher vibrational de-excitation probabilities at low energies. Whilst scattering at Cu(110) and Cu(100) produce pronounced peaks in transition probabilities at low collision energies (≈0.15 eV) with LDFA, scattering at Cu(211) and Cu(111) show a broader, flatter peak in transition probability at intermediate energies (0.25–0.3 eV), reflecting the complicated geometric effects at play. At high energies (>0.4 eV), transition probabilities decline across all surfaces. This is consistent with the rise in dissociative sticking, which removes trajectories from the scattering channel. In the case of Cu(100) and Cu(110), the collision energy dependence that arises from nonadiabatic effects may indeed be measurable in the future.

We further compare rovibrational de-excitation probabilities for H_2 and D_2 on Cu(111) at 0 K with prior theoretical work by Spiering and Meyer [15] (Fig. S15 within the SM [68]). While our adiabatic and LDFA results are in good agreement, we find much closer agreement between ODF and LDFA than previously reported. This may indicate that the previously reported fingerprint of specifically anisotropic nonadiabatic effects reported for Cu(111) may be an artifact of the low-temperature approximation [Eq. (3)] employed for ODF [50,65]. This finding would also be consistent with previous MDEF(ODF) simulations for H_2 scattering on Ag(111) [14,91]. Our results suggest that the largest difference between ODF and LDFA can be found for Cu(110) at low collision energies. Comparison between the 0 K and 300 K simulations further suggests that surface phonons play only a marginal role for scattering at Cu(111).

Taken together, these results show that while rovibrational de-excitation is a finely resolved and potentially sensitive observable, owing to the population being distributed over many rotational states, the absolute impact of electronic friction remains small across all surfaces studied and experimental resolution would have to significantly increase to be able to resolve subtleties that may arise from nonadiabatic effects.

E. Vibrational transition landscapes

To provide a comprehensive picture of the scattering dynamics across different Cu facets, we present an overview of the final state distributions in Fig. 10. These vibrational "transition landscapes" visualize the fate of H_2 molecules initially prepared in the rovibrational state $v = 2$, $J = 1$ as a function of collision energy at 300 K. Using stacked area plots from MDEF-ODF simulations, we distinguish between vibrationally (in)elastic scattering, as well as dissociation outcomes.

Each surface exhibits a characteristic landscape reflecting its underlying reactivity and vibrational mode-specific energy transfer behavior. For Cu(111), most molecules remain in vibrationally excited bound states at low energies, with dissociation becoming dominant only above ∼0.3−0.4 eV. In contrast, Cu(110) and Cu(211) show broader and more gradual transitions: vibrational de-excitation is more prominent at low energies, and dissociation occurs even at the lowest energies, consistent with their enhanced low-energy reactivity.

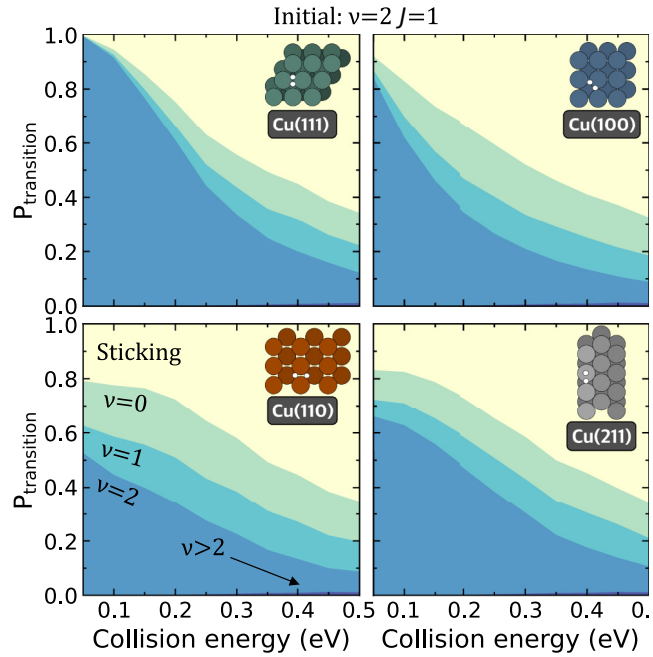

FIG. 10. Vibrational transition probabilities as stacked area plots for H_2 scattering at Cu surfaces (300 K). Final states after scattering of $H_2(v = 2, J = 1)$ are labeled. All final rotational quantum numbers are included. The vibrational excited population ($v > 2$) is very small. The probabilities were calculated using MDEF-ODF.

Cu(100) displays low energy reactivity and generally intermediate behavior between the response of Cu(111) and the broader distributions seen for Cu(110) and Cu(211).

The fraction of molecules that remain in the initial state decreases with increasing energy across all surfaces, as population flows into lower vibrational states and eventually into the dissociated channel. The population of molecules undergoing vibrational excitation ($v > 2$) is negligible, confirming that vibrational excitation is rare under these thermal conditions.

We also evaluated the equivalent transition landscapes using adiabatic and MDEF(LDFA) dynamics (Sec. XI within the SM [68]) and found only subtle quantitative differences. This further supports the conclusion that the role of electronic friction is minor in this system and does not dramatically reshape the outcomes of reactive scattering for H_2 on copper.

Together, these transition landscapes provide an intuitive and surface-specific summary of how energy and population flow through the scattering event. They highlight the influence of surface structure on dissociation thresholds, vibrational quenching, and the balance between elastic and inelastic channels, offering a concise visual representation of the full dynamical fingerprint for each facet.

IV. CONCLUSIONS AND OUTLOOK

In this work, we present machine learning surrogate models of electronic friction tensors that are transferable across different surface facets of copper. Both models are accurate representations of the underlying first-principles data. In combination with previously published machine learning

interatomic potentials, they constitute a framework to simulate quantum-state-resolved dynamics of H_2 scattering and dissociation on a range of Cu surfaces with high accuracy and with the ability to perform comprehensive statistical sampling. These models accurately reproduce reference data along representative scattering and dissociation pathways, enabling efficient and robust simulations that capture all nuclear degrees of freedom and weak nonadiabatic effects. The models are publicly available and constitute the current state-of-the-art in simulating reactive hydrogen chemistry on copper. The two EFT models represent an isotropic model based on the local density friction approximation and an anisotropic model based on first-order time-dependent perturbation theory or orbital-dependent friction.

Our simulations reproduce experimentally measured quantities and show an improved description over previous theoretical studies. By resolving the dynamics across initial rovibrational states and multiple Cu surface facets, we demonstrate that dissociative chemisorption remains largely adiabatic under thermal conditions, with electronic friction contributing only modest corrections. While subtle differences between LDFA and ODF emerge in specific regimes, particularly at low translational energies and on more corrugated surfaces, mode-specific friction effects remain small in this context. Notably, vibrational promotion varies significantly between facets and plays a key role in modulating reactivity at sub-barrier collision energies.

The machine learning models presented here provide a versatile framework for probing the role of nonadiabatic effects in surface reactions. While electronically nonadiabatic dissociation of H_2 appears to be weak, other observables such as kinetic energy loss distributions, ultrafast light-driven desorption probabilities, [92,93] or kinetic isotope effects [12,28,94] may offer more sensitive fingerprints of nonadiabaticity. The presented ML models will support future efforts to explore such fingerprints. Our machine-learning representation of the electronic friction tensor is readily generalizable to other adsorbates, coverages, and materials, offering a path toward unified, high-resolution models of reactive gas-surface dynamics in the presence of weak nonadiabatic effects.

ACKNOWLEDGMENTS

This work is partly based on W.G.S. Ph.D. thesis [95]. It was financially supported by The Leverhulme Trust (RPG-2019-078), the UKRI Future Leaders Fellowship programme (MR/S016023/1 and MR/X023109/1), and a UKRI Frontier Research Grant (EP/X014088/1). High-performance computing resources were provided via the Scientific Computing Research Technology Platform of the University of Warwick, the EPSRC-funded Materials Chemistry Consortium (EP/R029431/1, EP/X035859/1), and the UK Car-Parrinello Consortium (EP/X035891/1) for the ARCHER2 UK National Supercomputing Service, and the EPSRC-funded HPC Midlands+ computing center for access to Sulis (EP/P020232/1). We acknowledge helpful discussions with Alexander Spears.

DATA AVAILABILITY

The data that support the findings of this article are openly available [96,97].

[1] M. P. Andersson, F. Abild-Pedersen, I. N. Remediakis, T. Bligaard, G. Jones, J. Engbæk, O. Lytken, S. Horch, J. H. Nielsen, J. Sehested *et al.*, Structure sensitivity of the methanation reaction: H_2-induced CO dissociation on nickel surfaces, J. Catal. **255**, 6 (2008).

[2] D. Hollenbach and E. E. Salpeter, Surface recombination of hydrogen molecules, Astrophys. J. **163**, 155 (1971).

[3] M. Wilde, K. Fukutani, W. Ludwig, B. Brandt, J.-H. Fischer, S. Schauermann, and H.-J. Freund, Influence of carbon deposition on the hydrogen distribution in Pd nanoparticles and their reactivity in olefin hydrogenation, Angew. Chem. Int. Ed. **47**, 9289 (2008).

[4] S. M. Lee, K. S. Park, Y. C. Choi, Y. S. Park, J. M. Bok, D. J. Bae, K. S. Nahm, Y. G. Choi, S. C. Yu, N.-G. Kim *et al.*, Hydrogen adsorption and storage in carbon nanotubes, Synth. Met. **113**, 209 (2000).

[5] R. Kirchheim, Hydrogen solubility and diffusivity in defective and amorphous metals, Prog. Mater. Sci. **32**, 261 (1988).

[6] G. S. Higashi, Y. J. Chabal, G. W. Trucks, and K. Raghavachari, Ideal hydrogen termination of the Si(111) surface, Appl. Phys. Lett. **56**, 656 (1990).

[7] D. Haberer, D. V. Vyalikh, S. Taioli, B. Dora, M. Farjam, J. Fink, D. Marchenko, T. Pichler, K. Ziegler, S. Simonucci *et al.*, Tunable band gap in hydrogenated quasi-free-standing graphene, Nano Lett. **10**, 3360 (2010).

[8] N. Liu, L. Wu, Z. Qin, and D. W. Shoesmith, Roles of radiolytic and externally generated H_2 in the corrosion of fractured spent nuclear fuel, Environ. Sci. Technol. **50**, 12348 (2016).

[9] G. Ertl, Reactions at surfaces: From atoms to complexity (Nobel lecture), Angew. Chem. Int. Ed. **47**, 3524 (2008).

[10] D. J. Auerbach, J. C. Tully, and A. M. Wodtke, Chemical dynamics from the gas-phase to surfaces, Nat. Sci. **1**, e10005 (2021).

[11] D. Farías and R. Miranda, Diffraction of molecular hydrogen from metal surfaces, Prog. Surf. Sci. **86**, 222 (2011).

[12] L. Zhang, F. Nitz, D. Borodin, A. M. Wodtke, and H. Guo, Ring polymer molecular dynamics rates for hydrogen recombinative desorption on Pt(111), Precis. Chem. **3**, 319 (2025).

[13] R. J. Maurer, B. Jiang, H. Guo, and J. C. Tully, Mode specific electronic friction in dissociative chemisorption on metal surfaces: H_2 on Ag(111), Phys. Rev. Lett. **118**, 256001 (2017).

[14] R. J. Maurer, Y. Zhang, H. Guo, and B. Jiang, Hot electron effects during reactive scattering of H_2 from Ag(111): assessing the sensitivity to initial conditions, coupling magnitude, and electronic temperature, Faraday Discuss. **214**, 105 (2019).

[15] P. Spiering and J. Meyer, Testing electronic friction models: vibrational de-excitation in scattering of H_2 and D_2 from Cu(111), J. Phys. Chem. Lett. **9**, 1803 (2018).

[16] G.-J. Kroes, Computational approaches to dissociative chemisorption on metals: towards chemical accuracy, Phys. Chem. Chem. Phys. **23**, 8962 (2021).

[17] H. A. Michelsen, C. T. Rettner, and D. J. Auerbach, State-specific dynamics of D_2 desorption from Cu(111): The role of molecular rotational motion in activated adsorption-desorption dynamics, Phys. Rev. Lett. **69**, 2678 (1992).

[18] C. T. Rettner, Dynamics of the direct reaction of hydrogen atoms adsorbed on Cu(111) with hydrogen atoms incident from the gas phase, Phys. Rev. Lett. **69**, 383 (1992).

[19] C. T. Rettner, H. A. Michelsen, and D. J. Auerbach, Determination of quantum state-specific gas-surface energy transfer and adsorption probabilities as a function of kinetic energy, Chem. Phys. **175**, 157 (1993).

[20] E. Watts and G. O. Sitz, State-to-state scattering in a reactive system: $H_2(v = 1, J = 1)$ from Cu(100), J. Chem. Phys. **114**, 4171 (2001).

[21] L. C. Shackman and G. O. Sitz, State-to-state scattering of D_2 from Cu(100) and Pd(111), J. Chem. Phys. **123**, 064712 (2005).

[22] A. Hodgson, J. Moryl, and H. Zhao, Scattering of vibrationally excited H_2 from Cu(111), Chem. Phys. Lett. **182**, 152 (1991).

[23] M. J. Murphy and A. Hodgson, Adsorption and desorption dynamics of H_2 and D_2 on Cu(111): The role of surface temperature and evidence for corrugation of the dissociation barrier, J. Chem. Phys. **108**, 4199 (1998).

[24] K. Cao, G. Füchsel, A. W. Kleyn, and L. B. F. Juurlink, Hydrogen adsorption and desorption from Cu(111) and Cu(211), Phys. Chem. Chem. Phys. **20**, 22477 (2018).

[25] G. Anger, A. Winkler, and K. D. Rendulic, Adsorption and desorption kinetics in the systems D_2/Cu(111), D_2/Cu(110) and H_2/Cu(100), Surf. Sci. **220**, 1 (1989).

[26] P. Rasmussen, P. Holmblad, H. Christoffersen, P. Taylor, and I. Chorkendorff, Dissociative adsorption of hydrogen on Cu(100) at low temperatures, Surf. Sci. **287–288**, 79 (1993).

[27] J. Campbell and C. T. Campbell, The dissociative adsorption of H_2 and D_2 on Cu(110): activation barriers and dynamics, Surf. Sci. **259**, 1 (1991).

[28] F. Nitz, L. Zhang, N. Hertl, I. Rahinov, O. Galparsoro, A. Kandratsenka, T. N. Kitsopoulos, D. J. Auerbach, H. Guo, A. M. Wodtke, and D. Borodin, Thermal rates and high-temperature tunneling from surface reaction dynamics and first-principles, J. Am. Chem. Soc. **146**, 31538 (2024).

[29] H. A. Michelsen and D. J. Auerbach, A critical examination of data on the dissociative adsorption and associative desorption of hydrogen at copper surfaces, J. Chem. Phys. **94**, 7502 (1991).

[30] H. Michelsen, C. Rettner, and D. Auerbach, On the influence of surface temperature on adsorption and desorption in the D_2/Cu(111) system, Surf. Sci. **272**, 65 (1992).

[31] H. A. Michelsen, C. T. Rettner, D. J. Auerbach, and R. N. Zare, Effect of rotation on the translational and vibrational energy dependence of the dissociative adsorption of D_2 on Cu(111), J. Chem. Phys. **98**, 8294 (1993).

[32] C. T. Rettner, H. A. Michelsen, and D. J. Auerbach, Quantum-state-specific dynamics of the dissociative adsorption and associative desorption of H_2 at a Cu(111) surface, J. Chem. Phys. **102**, 4625 (1995).

[33] S. Kaufmann, Q. Shuai, D. J. Auerbach, D. Schwarzer, and A. M. Wodtke, Associative desorption of hydrogen isotopologues from copper surfaces: Characterization of two reaction mechanisms, J. Chem. Phys. **148**, 194703 (2018).

[34] M. J. Murphy, J. F. Skelly, A. Hodgson, and B. Hammer, Inverted vibrational distributions from N_2 recombination at Ru(001): Evidence for a metastable molecular chemisorption well, J. Chem. Phys. **110**, 6954 (1999).

[35] C. Díaz and R. A. Olsen, A note on the vibrational efficacy in molecule-surface reactions, J. Chem. Phys. **130**, 094706 (2009).

[36] J. C. Polanyi, Concepts in reaction dynamics, Acc. Chem. Res. **5**, 161 (1972).

[37] Y. Huang, C. T. Rettner, D. J. Auerbach, and A. M. Wodtke, Vibrational promotion of electron transfer, Science **290**, 111 (2000).

[38] B. C. Krüger, S. Meyer, A. Kandratsenka, A. M. Wodtke, and T. Schäfer, Vibrational inelasticity of highly vibrationally excited NO on Ag(111), J. Phys. Chem. Lett. **7**, 441 (2016).

[39] N. Shenvi, S. Roy, and J. C. Tully, Nonadiabatic dynamics at metal surfaces: Independent-electron surface hopping, J. Chem. Phys. **130**, 174107 (2009).

[40] G. Meng, J. Gardner, N. Hertl, W. Dou, R. J. Maurer, and B. Jiang, First-principles nonadiabatic dynamics of molecules at metal surfaces with vibrationally coupled electron transfer, Phys. Rev. Lett. **133**, 036203 (2024).

[41] M. Head-Gordon and J. C. Tully, Molecular dynamics with electronic frictions, J. Chem. Phys. **103**, 10137 (1995).

[42] Y. Li and G. Wahnström, Nonadiabatic effects in hydrogen diffusion in metals, Phys. Rev. Lett. **68**, 3444 (1992).

[43] J. I. Juaristi, M. Alducin, R. Diez Muiño, H. F. Busnengo, and A. Salin, Role of electron-hole pair excitations in the dissociative adsorption of diatomic molecules on metal surfaces, Phys. Rev. Lett. **100**, 116102 (2008).

[44] A. S. Muzas, J. I. Juaristi, M. Alducin, R. D. Muiño, G. J. Kroes, and C. Díaz, Vibrational deexcitation and rotational excitation of H_2 and D_2 scattered from Cu(111): Adiabatic versus nonadiabatic dynamics, J. Chem. Phys. **137**, 064707 (2012).

[45] A. C. Luntz, I. Makkonen, M. Persson, S. Holloway, D. M. Bird, and M. S. Mizielinski, Comment on "Role of electron-hole pair excitations in the dissociative adsorption of diatomic molecules on metal surfaces", Phys. Rev. Lett. **102**, 109601 (2009).

[46] C. L. Box, Y. Zhang, R. Yin, B. Jiang, and R. J. Maurer, Determining the effect of hot electron dissipation on molecular scattering experiments at metal surfaces, JACS Au **1**, 164 (2021).

[47] B. Hellsing and M. Persson, Electronic damping of atomic and molecular vibrations at metal surfaces, Phys. Scr. **29**, 360 (1984).

[48] M. Askerka, R. J. Maurer, V. S. Batista, and J. C. Tully, Role of tensorial electronic friction in energy transfer at metal surfaces, Phys. Rev. Lett. **116**, 217601 (2016).

[49] R. J. Maurer, M. Askerka, V. S. Batista, and J. C. Tully, Ab initio tensorial electronic friction for molecules on metal surfaces: Nonadiabatic vibrational relaxation, Phys. Rev. B **94**, 115432 (2016).

[50] C. L. Box, W. G. Stark, and R. J. Maurer, Ab initio calculation of electron-phonon linewidths and molecular dynamics with electronic friction at metal surfaces with numeric atom-centred orbitals, Electron. Struct. **5**, 035005 (2023).

[51] P. Spiering, K. Shakouri, J. Behler, G.-J. Kroes, and J. Meyer, Orbital-dependent electronic friction significantly affects the description of reactive scattering of N_2 from Ru(0001), J. Phys. Chem. Lett. **10**, 2957 (2019).

[52] C. L. Box, N. Hertl, W. G. Stark, and R. J. Maurer, Room temperature hydrogen atom scattering experiments are not a sufficient benchmark to validate electronic friction theory, J. Phys. Chem. Lett. **15**, 12520 (2024).
[53] J. Behler and M. Parrinello, Generalized neural-network representation of high-dimensional potential-energy surfaces, Phys. Rev. Lett. **98**, 146401 (2007).
[54] J. Behler, Representing potential energy surfaces by high-dimensional neural network potentials, J. Phys.: Condens. Matter **26**, 183001 (2014).
[55] V. L. Deringer, M. A. Caro, and G. Csányi, Machine learning interatomic potentials as emerging tools for materials science, Adv. Mater. **31**, 1902765 (2019).
[56] E. Kocer, T. W. Ko, and J. Behler, Neural network potentials: A concise overview of methods, Annu. Rev. Phys. Chem. **73**, 163 (2022).
[57] L. Zhu, Y. Zhang, L. Zhang, X. Zhou, and B. Jiang, Unified and transferable description of dynamics of H_2 dissociative adsorption on multiple copper surfaces via machine learning, Phys. Chem. Chem. Phys. **22**, 13958 (2020).
[58] W. G. Stark, J. Westermayr, O. A. Douglas-Gallardo, J. Gardner, S. Habershon, and R. J. Maurer, Machine learning interatomic potentials for reactive hydrogen dynamics at metal surfaces based on iterative refinement of reaction probabilities, J. Phys. Chem. C **127**, 24168 (2023).
[59] W. G. Stark, C. van der Oord, I. Batatia, Y. Zhang, B. Jiang, G. Csányi, and R. J. Maurer, Benchmarking of machine learning interatomic potentials for reactive hydrogen dynamics at metal surfaces, Mach. Learn.: Sci. Technol. **5**, 030501 (2024).
[60] Y. Zhang, R. J. Maurer, and B. Jiang, Symmetry-adapted high dimensional neural network representation of electronic friction tensor of adsorbates on metals, J. Phys. Chem. C **124**, 186 (2020).
[61] M. Sachs, W. G. Stark, R. J. Maurer, and C. Ortner, Machine learning configuration-dependent friction tensors in langevin heatbaths, Mach. Learn.: Sci. Technol. **6**, 015016 (2025).
[62] R. Drautz, Atomic cluster expansion for accurate and transferable interatomic potentials, Phys. Rev. B **99**, 014104 (2019).
[63] R. Drautz, Atomic cluster expansion of scalar, vectorial, and tensorial properties including magnetism and charge transfer, Phys. Rev. B **102**, 024104 (2020).
[64] M. Wijzenbroek, D. Helstone, J. Meyer, and G.-J. Kroes, Dynamics of H_2 dissociation on the close-packed (111) surface of the noblest metal: $H_2 + Au(111)$, J. Chem. Phys. **145**, 144701 (2016).
[65] M. Calandra and F. Mauri, Electron-phonon coupling and phonon self-energy in MgB_2: Interpretation of MgB_2 Raman spectra, Phys. Rev. B **71**, 064501 (2005).
[66] M. J. Puska and R. M. Nieminen, Atoms embedded in an electron gas: Phase shifts and cross sections, Phys. Rev. B **27**, 6121 (1983).
[67] N. Gerrits, J. I. Juaristi, and J. Meyer, Electronic friction coefficients from the atom-in-jellium model for $Z = 1 - 92$, Phys. Rev. B **102**, 155130 (2020).
[68] See Supplemental Material at http://link.aps.org/supplemental/10.1103/h7vd-94pk for a description of electronic structure convergence, machine learning model parameter optimization, and additional simulation data.
[69] L. Zhang, B. Onat, G. Dusson, A. McSloy, G. Anand, R. J. Maurer, C. Ortner, and J. R. Kermode, Equivariant analytical mapping of first principles Hamiltonians to accurate and transferable materials models, npj Comput Mater **8**, 158 (2022).
[70] I. Batatia, D. P. Kovacs, G. Simm, C. Ortner, and G. Csányi, MACE: Higher order equivariant message passing neural networks for fast and accurate force fields, *Advances in Neural Information Processing Systems*, Vol. 33 (Curran Associates, Inc., 2022), pp. 11423–11436.
[71] F. Nattino, C. Díaz, B. Jackson, and G.-J. Kroes, Effect of surface motion on the rotational quadrupole alignment parameter of H_2 reacting on Cu(111), Phys. Rev. Lett. **108**, 236104 (2012).
[72] J. P. Perdew, K. Burke, and Y. Wang, Generalized gradient approximation for the exchange-correlation hole of a many-electron system, Phys. Rev. B **54**, 16533 (1996).
[73] B. Hammer, L. B. Hansen, and J. K. Nørskov, Improved adsorption energetics within density-functional theory using revised Perdew-Burke-Ernzerhof functionals, Phys. Rev. B **59**, 7413 (1999).
[74] V. Blum, R. Gehrke, F. Hanke, P. Havu, V. Havu, X. Ren, K. Reuter, and M. Scheffler, Ab initio molecular simulations with numeric atom-centered orbitals, Comput. Phys. Commun. **180**, 2175 (2009).
[75] G. Henkelman, B. P. Uberuaga, and H. Jónsson, A climbing image nudged elastic band method for finding saddle points and minimum energy paths, J. Chem. Phys. **113**, 9901 (2000).
[76] W. C. Witt, C. van der Oord, E. Gelžinytė, T. Järvinen, A. Ross, J. P. Darby, C. H. Ho, W. J. Baldwin, M. Sachs, J. Kermode *et al.*, ACEpotentials.jl: A Julia implementation of the atomic cluster expansion, J. Chem. Phys. **159**, 164101 (2023).
[77] https://github.com/ACEsuit/ACEds.jl.
[78] https://github.com/ACEsuit/ACEpotentials.jl.
[79] https://github.com/ACEsuit/ACEfriction.jl.
[80] J. Gardner, O. A. Douglas-Gallardo, W. G. Stark, J. Westermayr, S. M. Janke, S. Habershon, and R. J. Maurer, NQCDynamics.jl: A Julia package for nonadiabatic quantum classical molecular dynamics in the condensed phase, J. Chem. Phys. **156**, 174801 (2022).
[81] https://github.com/NQCD/NQCDynamics.jl.
[82] A. J. Larkoski, D. G. Ellis, and L. J. Curtis, Numerical implementation of Einstein-Brillouin-Keller quantization for arbitrary potentials, Am. J. Phys. **74**, 572 (2006).
[83] A. C. Luntz and M. Persson, How adiabatic is activated adsorption/associative desorption?, J. Chem. Phys. **123**, 074704 (2005).
[84] G. J. Kroes, E. Pijper, and A. Salin, Dissociative chemisorption of H_2 on the Cu(110) surface: A quantum and quasiclassical dynamical study, J. Chem. Phys. **127**, 164722 (2007).
[85] M. Gostein and G. O. Sitz, Scattering of $H_2(v = 1, J = 1)$ from Cu(110): Survival probability versus incident energy, J. Vac. Sci. Technol. A: Vac. Surf. Films **14**, 1562 (1996).
[86] M. Gostein, H. Parhikhteh, and G. O. Sitz, Survival probability of H_2 ($v = 1$, $J = 1$) scattered from Cu(110), Phys. Rev. Lett. **75**, 342 (1995).
[87] L. Zhang, L. Zhu, and B. Jiang, Six-dimensional state-to-state quantum dynamics of H_2/D_2 scattering from Cu(100): Validity of site-averaging model, Chin. J. Chem. Phys. **35**, 143 (2022).
[88] L. Sementa, M. Wijzenbroek, B. J. van Kolck, M. F. Somers, A. Al-Halabi, H. F. Busnengo, R. A. Olsen, G. J. Kroes, M. Rutkowski, C. Thewes, N. F. Kleimeier, and H. Zacharias, Reactive scattering of H_2 from Cu(100): Comparison of dynamics

calculations based on the specific reaction parameter approach to density functional theory with experiment, J. Chem. Phys. **138**, 044708 (2013).

[89] J. Klimeš, D. R. Bowler, and A. Michaelides, Chemical accuracy for the van der Waals density functional, J. Phys.: Condens. Matter **22**, 022201 (2010).

[90] E. W. F. Smeets and G.-J. Kroes, Designing new SRP density functionals including non-local vdW-DF_2 correlation for H_2 + Cu(111) and their transferability to H_2 + Ag(111), Au(111) and Pt(111), Phys. Chem. Chem. Phys. **23**, 7875 (2021).

[91] Y. Zhang, R. J. Maurer, H. Guo, and B. Jiang, Hot-electron effects during reactive scattering of H_2 from Ag(111): the interplay between mode-specific electronic friction and the potential energy landscape, Chem. Sci. **10**, 1089 (2019).

[92] J. I. Juaristi, M. Alducin, and P. Saalfrank, Femtosecond laser induced desorption of H_2, D_2, and HD from Ru(0001): Dynamical promotion and suppression studied with ab initio molecular dynamics with electronic friction, Phys. Rev. B **95**, 125439 (2017).

[93] G. Füchsel, T. Klamroth, S. Monturet, and P. Saalfrank, Dissipative dynamics within the electronic friction approach: the femtosecond laser desorption of H_2/D_2 from Ru(0001), Phys. Chem. Chem. Phys. **13**, 8659 (2011).

[94] Y. Litman, E. S. Pós, C. L. Box, R. Martinazzo, R. J. Maurer, and M. Rossi, Dissipative tunneling rates through the incorporation of first-principles electronic friction in instanton rate theory. II. Benchmarks and applications, J. Chem. Phys. **156**, 194107 (2022).

[95] W. G. Stark, Machine learning models for gas-surface dynamics, Ph.D. thesis, University of Warwick, 2024.

[96] https://github.com/wgst/ml-gas-surface.

[97] W. G. Stark, "wgst/ml-gas-surface: Release v1.0", Zenodo, https://doi.org/10.5281/zenodo.15720346.